Formation of nitrile species on Ag nanostructures supported on a-Al_2O_3: a new corrosion route for silver exposed to the atmosphere

R.J. Peláez,[1] J. P. Espinós,[2] C.N. Afonso[1]

[1]Laser Processing Group, Instituto de Optica, CSIC, Serrano 121, 28006, Madrid, Spain

[2]Surface Analysis Lab, Instituto de Ciencia de Materiales de Sevilla, CSIC-US, Américo Vespucio 49, 41092, Sevilla, Spain

ABSTRACT

The aging of supported Ag nanostructures upon storage in ambient conditions (air and room temperature) for 20 months has been studied. The samples are produced on glass substrates by pulsed laser deposition (PLD) by depositing first a 15 nm thick buffer layer of amorphous aluminum oxide (a-Al_2O_3) followed by PLD of Ag. The amount of deposited Ag ranges from that leading to a discontinuous layer up to an almost percolated layer with thicknesses < 6 nm. Some regions of the as grown silver layers are converted into round, isolated and with up to ~25 nm diameter nanoparticles (NPs) by laser induced dewetting. The plasmonic, structural and chemical properties of both as grown and laser exposed regions upon aging have been followed through extinction spectroscopy, scanning electron microscopy and X-ray photoelectron spectroscopy respectively. The results show that the discontinuous as grown regions are optically and chemically unstable and that the metal becomes oxidized faster the smaller the amount of Ag. The corrosion leads to the formation of nitrile species due to the reaction between NO_x species from the atmosphere adsorbed at the surface of Ag and hydrocarbons adsorbed in defects at the surface of the a-Al_2O_3 layer during the deposition of the Ag nanostructures by PLD that migrate to the surface of the metal with time. The nitrile formation thus results in the main oxidation mechanism and inhibits almost completely the formation of sulphate/sulphide. Finally, the optical changes upon aging offer an easy to use tool to follow the aging process. They are dominated by an enhanced absorption in the UV side of the spectrum and a blue-shift of the surface plasmon resonance that are respectively related to the formation of a dielectric overlayer on the Ag nanostructure and changes in the dimensions/features of the nanostructures both due to the oxidation process.

INTRODUCTION

Nanostructures and nanoparticles (NPs) are characterized by their high surface to volume ratio that is responsible for their special properties when compared to those of the bulk material [1]. One of the most widely studied phenomenon is the resonant optical absorption of noble metal NPs. It is due to the excitation of surface plasmon resonances (SPRs) that are exploited for sensing, photovoltaic or metamaterials [2–4]. Silver nanostructures are the most attractive ones since their SPR is stronger than that of other noble metals like gold because it is well separated from interband transitions. SPRs of supported Ag NPs have been demonstrated to improve the efficiency of solar cells, and to lead to metamaterials for silver subwavelength slit gratings or plasmon-active tips-enhanced for Raman spectroscopy. However, surface tarnishing and/or chemical degradation of silver nanostructures upon exposure to the atmosphere decrease the quantum efficiency of the solar cells, reduce the extraordinary optical transmission of the metamaterials and limits the field enhancement of tips used for sensing [5–9].

Surface tarnishing of Ag is known since very long [10,11], and the main constituent reported upon exposure of silver to the atmosphere has been silver sulfide [12]. Although only a very thin layer is formed, it induces a dielectric overlayer that influences the optical response. The optical changes include the damping and shift of the SPR wavelength. However, different senses have been reported for the shift that have been suggested to be related to the NPs features: while Ag-nano objects with dimensions of tens up to hundreds of nm exhibit typically a red-shift [13,14], Ag NPs with small diameters exhibit a blue-shift [15]. Furthermore, the chemical activity of the latter type of Ag NPs is known since very long to depend on the supporting substrate [16].

Metal NPs on oxide supports constitute an important class of heterogeneous catalysts that have been studied for a longtime [1,17]. There are support interactions that lead to a modification of the reaction and adsorption properties of the supported NPs. Most of these studies have been performed on crystalline substrates that were either single crystals or epitaxially grown films that require special conditions to be produced. Very little has been reported on the use of their amorphous counterparts that generally require no specific conditions or high temperatures in their production. For this work, we have selected amorphous aluminum oxide (a-Al_2O_3) as support for the metal nanostructures because on the one hand, we have recently reported that Ag NPs on a-Al_2O_3 support become strongly oxidized under atmospheric conditions, sulfurization being negligible [15]. On the other hand, the adsorption of Ag on Al_2O_3 is known to be highly sensitive to its surface termination, being weak when it is Al or hidroxilated or water terminated surfaces and strong when it is O-terminated[18,19]. When compared to the crystalline material, a-Al_2O_3 has a lower surface energy and more surface defects that can favor the adsorption of species [20,21]. Last but not least, Al_2O_3 has a high refractive index, high dielectric constant with low leakage current [22,23] and an exceptional wear and scratch resistance [24] that make it very attractive for a wide range of applications in optical communication networks, microelectronics and coatings.

In order to provide a deeper understanding of the different corrosion mechanisms of Ag nanostructures on a-Al_2O_3 supports and clarify whether there is any dependence on the NPs dimension, we have monitored the plasmonic reponse, the morphological features and the chemical composition of Ag nanostructures supported on a-Al_2O_3 exposed to the atmosphere along 20 months. These nanostructures are fabricated by pulsed laser deposition (PLD) by producing first a supporting a-Al_2O_3 layer followed by the deposition of different amounts of Ag. Part of the nanostructured

layers are converted into isolated and almost round NPs having up to ~25 nm diameter by laser induced dewetting. A widespread range of dimensions and shapes are thus studied under the same aging conditions: flat (thickness < 6 nm) nanostructures ranging from a discontinuous layer up to an almost percolated layer and almost round and isolated NPs having diameters up to ~ 25 nm . The results obtained agree well with those reported earlier for flat nanostructures [15] and support a new corrosion route based on the reduction of NO_x from atmosphere to form Ag-CN species at room temperature in which the a-Al_2O_3 support plays an essential role.

EXPERIMENTAL

The samples are produced by PLD using an ArF excimer laser (λ=193 nm, τ=20 ns full width half maximum (FWHM)), focused at an angle of incidence of 45° on the target at a fluence of ~2.7 J cm^{-2}. The substrates are standard cover glass slides held at room temperature that are rotated along an axis parallel to the plasma expansion axis and shifted a few mm in order to produce a homogenous deposit over an area >1 cm^2. The ablation is performed in vacuum (P~10^{-6} mbar) by first focusing the laser beam to the surface of a high purity ceramic Al_2O_3 target to produce a 15 nm thick buffer layer of a-Al_2O_3. Without breaking the vacuum, the laser is then focused to a 99.99% Ag target during 3 different times, in order to produce layers with effective thicknesses of 1.6 nm, 3.7 nm and 5.9 nm. Finally, the vacuum chamber is generally filled with 99.999% N_2 to bring it to atmospheric pressure. A second series of three samples are produced using the same conditions of the thinnest and thickest Ag layers but with no buffer layer, i.e. the Ag is directly deposited on glass. These samples will from now on referred to as reference samples. Unless otherwise specified, all results presented will refer to samples having the a-Al_2O_3 buffer layer.

In order to modify the initial nanostructure of the samples, we have used the same laser combined with a beam homogenizer that leads to a constant intensity (within 5%) over ~4x4 mm^2 square regions, to irradiate regions of the thickest and thinnest samples in air immediately after deposition. We have used single pulses of fluences in the range 106-197 mJ cm^{-2}.

The samples are stored in air within single wafer shippers (47 mm diameter, ~3 cm^3) made of natural polypropylene (Entegris). They are stored in Madrid, where the optical characterization starts immediately after laser processing and is repeated several times along 15 months. The samples travel 3 times to Sevilla where they stayed for chemical and structural characterization during the periods of days 14-91, 218-309 and from 441 on. These periods will be referred to from now on as 0.5 m, 7 m and 15 m where **m** stands for months. In addition, the optical results assigned to these periods correspond to measurements performed just before the period starts. Further details on the production and laser irradiation procedures as well as on the evolution of optical and structural properties of similar samples upon aging can be found elsewhere [15,25].

The optical response of both as grown and laser exposed regions has been analyzed through the extinction spectra calculated as $ln(1/T(\lambda))$, where $T(\lambda)$ is the transmittance measured at normal incidence, using a Cary 5000 dual beam spectrophotometer. The structural properties are characterized by scanning electron microscopy (SEM) in a Zeiss CrossBeam 1540XB microscope. The chemical composition of the surface is determined by X-ray photoelectron spectroscopy (XPS) using a SPECS Phoibos 100 DLD spectrometer and working in the pass energy constant mode at a value of 35 eV. The XPS spectra were excited with unmonochromatic Mg Kα ($h\upsilon$ = 1253.6 eV) radiation. The intensity of the main photoemission peaks detected, i.e. Al_{2p}, O_{1s}, Ag_{3d}, C_{1s}, N_{1s} and S_{2p}, are used to calculate the chemical composition of the

surface. We have used Shirley type backgrounds to determine the area under the peaks [26], that are finally corrected for the escape depth of electrons [27], the photoionization cross sections of each photoelectron signal [28] and the transmission function of the analyzer [29].

The modified Auger parameter (α') that is a key factor for determining the chemical state of silver is calculated from the binding energy of the $Ag_{3d5/2}$ peak and the kinetic energy of the Ag_{M4VV} Auger peak. The percentage of metal Ag(0) and oxidized Ag(I) is derived from the Ag_{MNN} Auger signals rather than from the more intense Ag_{3d} signals because the dependence of the shape and energetic features of the former on the chemical state of Ag is stronger [30]. As Ag_{MNN} reference spectra for pure Ag(0), we have used the one recorded from a ~6 nm thick Ag layer deposited by thermal evaporation in the XPS chamber, under ultrahigh vacuum conditions ($P<10^{-9}$ mbar), and measured without breaking the vacuum. This reference spectrum was then subtracted from the experimental ones obtained in the samples studied in this work, in order to fully remove the contribution of the metallic component. In order to calculate the degree of silver oxidation, the resulting Ag_{MNN} spectra were then compared to the spectrum reported elsewhere [15] for a 1.6 nm thick Ag sample on a-Al_2O_3 that was prepared following the same procedure than in the present work. This sample was completely oxidized after 25 months in similar aging conditions and will from now on referred to as oxidized reference sample.

Further information on the chemical composition of a selection of regions and samples is obtained by Raman spectroscopy with a LabRam spectrophotometer (Horiba Jobin Yvon), by exciting with the non polarized beam from an Ar laser (λ = 514.5 nm) at their front face, and collecting the backscattered light. We have used the minimum power required to obtain signals in order to prevent any possible transformation.

RESULTS

Figure 1a shows the extinction spectrum recorded at 0.5 m from the as grown region of the thickest sample. It exhibits a broad band peaking around 613 nm related to the SPR of the as grown region of the metal nanostructure that consists of irregular and almost percolated silver NPs, as seen in Figure 1c. Upon laser irradiation, the SPR narrows and shifts blue (see also Figure 1a), the amount of the shift depending on fluence as shown in the inset of Figure 1a, where the wavelength position of the SPR as a function of fluence is plot. The largest shift occurs for fluences in the range 120-152 $mJcm^{-2}$ and is related to the complete break of the as grown layer into isolated irregular NPs for low fluences (Figure 1d) and into almost round and well isolated NPs for higher fluences (Figures 1e and 1f). Unless otherwise specified, the results presented from now on for laser exposed regions refer to regions irradiated with a fluence of 152 $mJcm^{-2}$. Figure 1a also shows the spectra of both the as grown and laser exposed regions of the same sample at 15 m, where it is seen that they are similar to those recorded at 0.5 m. The inset in Figure 1a shows that the SPR wavelength of the as grown regions at 15 m follows the same dependence on fluence than that at 0.5 m, although the values are slightly blue-shifted as it becomes evident in the spectrum.

Figure 1b includes de same type of spectra than Figure 1a but for the thinnest sample. The spectrum of the as grown region at 0.5 m exhibits a narrower band than that of the same region of the thickest sample, peaking around 505 nm. This result is consistent with the discontinuous character of the sample or its smaller effective thickness. Upon laser irradiation, the SPR also narrows and shifts blue. At 15 m, significant changes are observed in the as grown region: a blue-shift of the SPR in the as grown region and a strong increase of the extinction at the UV edge of the spectrum,

the latter also occurring in the laser exposed region. It is worth pointing out here that results for wavelengths shorter than 300 nm are meaningless due to the absorption of the glass substrate.

The detailed values of the SPR wavelength of all studied as grown and laser exposed regions as a function of aging time are shown in Figure 2. It is seen that the as grown regions show a continuous blue-shift as time progresses, the lower the metal content the higher the shift. The laser exposed regions show much smaller shift that becomes almost negligible for the thickest sample.

Figure 3 shows SEM images of all studied as grown regions at 0.5 m, 7 m and 15 m. It is seen that the nanostructure evolves from almost isolated small NPs (thinnest sample, Figure 3a), to bigger and coalesced NPs (intermediate thickness sample, Figure 3d) to an almost percolated structure (thickest sample, Figure 3g). Elongated structures appear to develop on top of the initial nanostructure at 7 m in the thinnest sample (Figure 3b), while similar features are seen in the intermediate thickness sample at 15 m (Figure 3f) and never observed in the thickest one (Figure 3g-i). The average Feret length and aspect ratio of these elongated structures are shown in Figure 4a as a function of aging time. It is seen that once they appear their length changes little with time and they are ~5 times longer in the intermediate thickness sample (Figure 3f) than in the thinnest sample. The present results are consistent with our earlier observations in similarly prepared discontinuous samples, in which similar elongated structures were observed between 7 m and 10 m for an effective Ag thicknesses ≤ 4.3 nm [15].

The discontinuous character of the samples leads to charging effects during SEM observations that prevented us to collect quality images at high magnifications. This made image processing and statistics of dimensions of the underlying nanostructure in the as grown regions generally not reliable, particularly for the thinnest sample, because

the process requires defining the NPs contours and the magnification used limits the smallest NP detectable to ~10 nm. Having in mind these limitations, we have determined the coverage and the mean Feret in-plane diameter of the underlying nanostructure for the 5.9 nm and 3.7 nm thick samples. The results are respectively plot in Figures 4b and 4c as a function of aging time. It shows that the coverage decreases in the range 0.55-0.40 during the studied period, the smaller the amount of Ag the higher the decrease. In addition, while the dimensions of the underlying nanostructure of the thickest sample remain almost constant (diameter ~27 nm), those of the intermediate thickness sample decreases a factor of 2 at 7 m and remains approximately constant afterwards. These results suggest that agglomeration of the silver occurs upon aging, the smaller the amount of silver the higher the agglomeration.

Figure 5 shows SEM images of laser exposed regions of the two extreme thickness samples at 0.5 m (Figures 5a and 5c) and 15 m (Figures 5b and 5d). For the thinnest sample (Figures 5a and 5b), the laser produces the agglomeration of Ag into NPs that are bigger than in the as grown region (compare Figure 5a to Figure 3a) leading to a reduction of the number density of NPs. In addition, big and almost black areas appear that relate to the break of the a-Al_2O_3 buffer layer [25,31]. For the thickest sample (Figures 5c and 5d), the laser produces the break-up of the layer into round NPs as described in Figure 1 and the NPs show negligible changes upon aging. Using the same criteria than for the as grown regions, the mean in-plane Feret diameter of the round NPs in the laser exposed region resulted to be very similar to that in the as grown region (see Figure 4c). Instead, the coverage in the laser exposed region is almost a factor of two smaller at 0.5 m and shows little variation upon aging. These results are consistent with the obvious shape changes observed in the morphology of the NPs (Figure 1 and Figure 3) and the SPR (Figure 1) that are related to a re-organization of

the silver into round and thicker NPs. At this point, it should be worth to point out that in spite of the in-plane dimensions of the NPs in as grown and laser processed regions are similar, their out-of-plane dimension is very different. Whereas the former is in average the layer thickness (i.e. the NPs are flat), the latter is similar to the in-plane dimension of the NPs (i.e. the NPs are approximately spherical).

XPS allows us to analyze the surface composition of the NPs as well as the uncovered regions of the a-Al_2O_3 support, thus providing the oxidation state of Ag and the ambient contaminants adsorbed. Figure 6 shows the XPS spectra of as-grown regions of the thinnest sample at 0.5 m and 7 m as illustrative surveys. The spectra are dominated by the photoemission peaks from silver (Ag_{3d}, Ag_{3p}, Ag_{MNN}, Ag_{4s}, Ag_{4p}, Ag_{4d5s}) and carbon (C_{1s}, C_{KVV}. Photoemission peaks from the elements composing the a-Al_2O_3 support (Al_{2p}, Al_{2s}, O_{1s} and O_{KVV}) appear as medium size peaks since they are partially hidden by the Ag NPs on top and the aforementioned carbon adsorbates. In addition, weaker peaks that initially are not visible in the scale selected for Figure 6 appear at a binding energy of ~400 eV related to nitrogen (N_{1s} level) and in the range 168-162 eV related to sulfur species (S_{2p} level) upon long aging times. Even weaker peaks from Si^{+4} species -Si_{2p} (103 eV) and Si_{2s} (156 eV) are also found for the case of the laser exposed region of the thinnest sample, that support further the interpretation that the black areas observed in Figures 5a and 5b relate to the break of the a-Al_2O_3 buffer layer by the laser exposure. The spectrum of the same region of the same sample at 7 m is also included and shows changes in the intensity and/or shape of the peaks.

Figure 7 shows separately the Ag related spectral regions (Ag_{3d} and Ag_{M4VV}) of the XPS spectra at 0.5 m for both as-grown and laser exposed regions of all studied samples. The peaks are quite narrow (FWHM in the range 1.3-1.6 eV for $Ag_{3d5/2}$ and 2.90 eV for Ag_{M4VV}) and the shapes are identical to those of pure metallic Ag. These

results thus support that Ag is not oxidized at 0.5 m. Table 1 includes the binding energy of the $Ag_{3d5/2}$ peak and the kinetic energy of the Ag_{M4VV} peak as well as their FWHM for all studied samples and regions. It is seen that the FWHM of the $Ag_{3d5/2}$ peak decreases as the amount of silver increases and it is generally smaller for the laser exposed region than for the corresponding as-grown one. Since it is known that the smaller the Ag NPs the higher the width of the photoemission peak [32], this result agrees with the SEM images in Figure 3 and Figure 5 and the dimensions from them extracted in spite of the limitations described above.

The features of the Ag photoelectron signals change over time in a degree that depends on the silver content, the strongest changes being observed in the thinnest sample. The main changes that appear upon aging in the Ag related XPS peaks are shown in Figure 8 where the Ag_{3d} and Ag_{MNN} regions of the spectra recorded in as grown regions of the thinnest sample are shown at the studied aging stages. While the $Ag_{3d5/2}$ peak only experiences a slight shift to higher binding energies upon aging (Figure 8a), the spectra of the Ag_{MNN} related region (Figure 8b) exhibit very significant changes. The binding energies of the $Ag_{3d5/2}$ peak of as grown and laser exposed regions of the thinnest sample shift respectively to 368.9 eV and 368.60 eV at 15 m. This shift becomes almost negligible (~0.1±0.05 eV) in the rest of studied samples (Table 1). Instead, the FWHM of this peak increases significantly upon aging in all cases with the exception of the thickest sample.

The described changes in the thinnest sample indicate that the electronic structure of the nanostructure, which is determined by their mean dimensions/shape, their electronic interaction with the substrate and/or the chemical state of the composing Ag atoms, has been modified. Indeed, the evolution with time of the Ag_{MNN} region for the thinnest sample (Figure 8b) is clearly indicating that some of the Ag atoms forming

the NPs become oxidized to Ag(I) upon aging. In this sense, the spectra of the oxidized reference sample have been also included in Figure 8 as a reference. Following the method described in the experimental section, the percentages of Ag(0) and Ag(I) have been estimated for all studied samples and regions and the results are also summarized in Table 1. It is worth to notice that both as-grown and laser exposed regions of the thinnest sample become highly oxidized at 7 m, while both regions of the thickest one remain metallic even after 15 m. The as grown region of the intermediate thickness sample becomes partially oxidized at 15 m. These results suggest that the smaller the amount of silver the higher the oxidation degree and the sooner it occurs.

Since sulfidation due to reaction of surface Ag atoms with H_2S and COS in the atmosphere has been the most widely reported mechanisms for explaining atmospheric tarnishing of Ag nanostructures upon time [11,12], we have also carefully analyzed the presence of S upon aging through the S_{2p} photoemission signal. The corresponding spectral region is included in Figure 9a where it is seen that a weak peak develops at a binding energy of 161.75 ± 0.1 eV at 7 m that is related to sulphide species. In addition, a much weaker peak starts to appear at 15 m around 168.5± 0.1 eV that could be related to sulphate species. While the sulphide related peak develops to different extents in all samples and regions at different stages, the intensity of sulphate species signal is below the detection limit in all other studied regions and samples. The quantitative data extracted from these spectra for all studied samples, regions and aging stages are also included in Table 1.

The quantification of the intensity of the different photoemission signals, after integration of the area below the main peaks and correction by proper sensitivity factors [29], allows us to determine the surface composition upon aging. The results are also included in Table 1, where the surface composition is expressed in atomic %. Since Ag

deposits on top of the a-Al_2O_3 support and the mean free path of the photoemitted electrons is small, the Ag_{3d} to Al_{2p} intensity ratio (Ag/Al) provides information on the coverage degree of Ag over the a-Al_2O_3, as well as the amount of Ag in the layer. This ratio is plot in Figure 10 as a function of the effective thickness for both as-grown and laser exposed regions as well as for 0.5 m and 7 m (see also Table 1). Regardless the aging stage, the Ag/Al determined for as grown regions increases monotonously as the amount of silver increases, as expected for a gradual increase of the coverage of the a-Al_2O_3 support when more silver is deposited on top of it. When comparing Ag/Al in as grown to laser exposed regions, a strong decrease is observed consistently with the dewetting process promoted by the laser induced melting. These results are in excellent agreement with the coverage values included in Figure 4b that were deduced from the SEM images. Finally, the Ag/Al ratio increases in all cases upon aging, the highest relative increase being observed between 0.5 m and 7 m in the laser exposed regions. As aging time increases further, this ratio tends to saturate, the variation being of ~20 % at the most.

Although the S atomic content seems to slightly depend on the NPs size, it is lower than 0.4% atoms and thus the S/Ag ratio remains ≤ 0.04 after 15 m. Since the two studied regions of the thinnest sample are already extensively oxidized (see Table 1) at 15 m, it can be concluded that sulfidation is far from being the main mechanism responsible for the oxidation of silver. This conclusion totally agrees with recent works [15,33]. Table 1 also includes the content of oxygen normalized to the content of the two metallic elements present at the surface, i.e. Al and Ag. The O_{1s} signal is a single broad band peaking at 532.0 ±0.05 eV (FWHM=2.9 eV) and since oxygen could be linked to aluminum, carbon, silver and even to Si from the glass substrate, we did not attempted to fit this signal. If the oxidation of Ag(0) to Ag (I) seen upon aging were

related to the bond of Ag to oxygen species, the O/(Al+Ag) should increase upon aging provided that Figure 10 shows that Ag/Al increases upon aging. However, Table 1 shows that O/(Al+Ag) exihibit the opposite behavior upon aging thus suggesting that Ag(I) should be bonded to non oxygenated anions rather than to oxygen forming silver oxides.

Overall, Table 1 evidences that the main element at the surface is C having concentrations ranging from 33.5% to 55.7%. The C_{1s} related region in the XPS spectra is shown in Figure 9b. They show a single asymmetric peak with a longer tail at the high binding energy side with little changes in the binding energy position upon aging. In spite of its apparent simplicity, four components are needed to fit these spectra properly for all the spectra acquired at different aging stages, as illustrated in Figure S1 of supporting information for the as-grown region of the thinnest sample at 0.5 m. In order to have chemical consistency, the four components have the same shape. The peak energy position and FWHM are included in Table 2 for all aging stages. The first component, C_I at 284.65 ±0.05 eV, corresponds to C-H and C-C species in both aliphatic and aromatic organic molecules. They are very common adsorbates found on the surface of any kind of solid exposed to the atmosphere for long and are usually referred to as “adventitius carbon”. In spite of the great care taken in the storage, the surface concentration of these species is very high irrespective of the thickness or the treatment. The components at higher binding energies are usually assigned to C atoms bonded to heteroatoms (O, N, S, Cl, F, …), the higher the electronegativity of the heteroatom or the higher the bond order, the higher the binding energy. The next two components, C_{II} at 285.35 ± 0.05 eV and C_{III} at 286.7 ± 0.1 eV, should be assigned to C atoms singled or multiple bonded to N (amines, amides, nitriles, …) and single bonded to O (alcohols, ethers, …), respectively. The last component C_{IV}, at 288.4 ± 0.3 eV,

should be ascribed to C=O species (cetones, aldehides, esters, …). Note that C_{II} is the only component whose relative intensity changes significantly over aging.

Finally, the most unexpected result with respect to surface composition is the appearance of nitrogen upon aging with surface concentrations that can be up to 6.2% (see Table 1). No chemicals containing nitrogen have been used for the preparation of the samples or during their storage. In addition, supplementary analyses have shown that no N_{1s} signal is ever detected either on the surface of the a-Al_2O_3 support or on the surface of the bare glass substrates. Furthermore, no nitrogen was detected either in a sample in which the silver NPs were fully buried in a-Al_2O_3 or were supported directly on the glass substrate [15]. Figure 11 shows N/Ag as a function of aging time for the different samples and regions studied. It is seen that the N signal appears at 7 m and becomes higher at 15 m, this increase being higher the smaller the amount of silver (see also Table 1). In order to analyze if N keeps increasing with time, the as grown regions of the samples where measured again at 20 m and Figure 11 shows that the N/Ag ratio tends to saturate after 15 m.

The evolution of the N_{1s} region upon aging is illustrated in Figure 9c for the case of the as grown region of the thinnest sample. The photemission signal is quite symmetric and narrow (FWHM=1.55 ±0.05eV), which suggests that it is caused by a single chemical species. The binding energy position, 399.1 ±0.1 eV, is compatible with nitrogen bonded to silver, aluminum [34] or carbon [35–38] and excludes the possibility of N bonded to oxygen. The N_{1s} binding energy in binary aluminum nitrides films has been reported to range between 399.7 eV and 397.8 eV, depending on its purity and microstructure [39,40], while for nitrogen coordinated to other metals (i.e. silver nitride) this energy range could be even higher depending on the nature of the metal and the bonding structure (amides, imides or nitrides) [34]. However, silver nitride is an

extremely explosive compound that slowly decomposes at room temperature [41]. It has never been synthesized by dry methods and, to our knowledge, it has never been studied by XPS or any other ultra-high-vacuum analysis technique, very likely due to its instability under vacuum and X-ray illumination. Finally, the bonding configurations of carbon-nitrogen systems can be very complex (amines, nitriles, amides, …) and the binding energies can range between 398 and 401 eV[42].

In order to investigate further the chemical nature of the detected nitrogen species, a selection of samples / regions has been characterized by Raman spectroscopy. Figure 12 shows the spectra of as-grown regions of the thinnest and thickest samples at 7 m together with the spectra of the corresponding reference samples on glass, i.e. same silver content but no a-Al_2O_3 buffer layer. Although the samples have undergone the same aging process, nitrogen species were only sharply detected by XPS on the surface of the samples in which Ag was on a-Al_2O_3 supports. The spectra in Figure 12 evidence several broad signals in the 500-3200 cm^{-1} energy range. The two more intense bands, at 1565±5 and 1355±5 cm^{-1}, are ascribed to C=C bond vibrations caused by in-plane vibrational modes of sp^2 C=C bonds in amorphous carbon [43]. They are usually referred to as “G band”, where G means graphitic, and “D band”, where D means disordered. The bands at 2905±5 cm^{-1} and 670-800 cm^{-1}, also found in amorphous carbon, are ascribed to the stretching and bending vibrational modes of C-H bonds, respectively. In addition, a new band peaking at 2138±2 cm^{-1} is found in the samples having Ag on a-Al_2O_3 whose intensity is much higher for the case of the thinnest sample. This band should be assigned to the stretching vibrational mode of nitrile (also known as “cyanide”) species, -C≡N and its energy is known to be slightly dependent on the nature of the metallic species they are linked to and the adsorption mode [44]. More specifically this band has been reported at 2142 cm^{-1} for nitrile species bonded to Ag^+

through a carbon atom (Ag-C≡N), at 2165 cm^{-1} in bulk AgCN for $Ag(CN)_2^-$ species in aqueous solutions [45], and at 2130 cm^{-1} when $(CN)^-$ is adsorbed on Ag NPs supported on Al_2O_3 [46,47]. In addition, for nitrile species bonded to Al^{3+}, two vibrational bands **ν**(CN) have been reported at 2165 cm^{-1} and 2155 cm^{-1} [48].

DISCUSSION

The main and unexpected result of this work is the appearance of nitrogen on the surface of the samples upon aging. Before our earlier work [15], this phenomenon has been reported upon aging at room temperature and atmospheric conditions to our knowledge neither in this system nor in other common metal/oxide (M/BO_x) systems, the latter systems being widely used as supported heterogeneous catalysts where M=Pt, Pd, Au, Ni,… and BO_x=Al_2O_3, SiO_2, TiO_2, CeO_2, ZrO_2. [1] Furthermore, we have earlier reported [15] that the incorporation of nitrogen was almost negligible when the Ag nanostructures were prepared directly on a bare glass substrate, i.e. with no a-Al_2O_3 buffer layer. In this work, we have confirmed further this result through the test Ag nanostructures produced directly on glass and undergoing the same aging conditions than the ones on a-Al_2O_3 studied in this work.

The main findings of this work with respect to the incorporation of nitrogen together with those achieved in our earlier work [15] can be summarized as follows:

- Initially (at 0.5 m), the surface of all studied samples and regions only contains metallic Ag and is free of any trace of nitrogen.
- Upon aging, the surface of silver becomes oxidized to Ag(I), the smaller the amount of silver the faster the oxidation and the higher the percentage of oxidized Ag atoms.
- Ag(I) is bonded to non oxygenated anions rather than to oxygen forming silver oxides.

- Nitrogen appearance occurs sooner and its content is higher the smaller the amount of silver (at 7 m in the thinnest studied sample). In addition, nitrogen tends to saturate after 15 m.

- Nitrogen is not observed either in bare a-Al_2O_3 supports or glass substrates upon aging as well as in samples having the metal NPs buried in a-Al_2O_3.

- Nitrogen is only clearly detected on the surface of samples in which Ag is on a-Al_2O_3 supports.

- The nitrogen that appears at the surface is forming nitrile species.

The above list of evidences suggests that the observed nitrile species are bonded to Ag(I) atoms located at the surface of the silver nanostructures and are produced during their storage in atmospheric conditions rather than during their fabrication. A first hypothesis to explain the origin of these species is surface pollution of samples. To analyze this hypothesis, we have measured the composition of both the bare and a-Al_2O_3 coated glass substrates by XPS as well as the inner and outer surfaces of the plastic containers used for the storage of the samples. No traces of nitrogen were ever detected. We have even revised thoroughly the experimental set up and the preparation and storage protocols. No sources of nitriles (C_2N_2, HCN, inorganic cyanides, or organic nitrile solvents as acrylonitrile, acetonitrile, etc.) could be found in the immediate vicinity of the samples. Finally, we have repeated the preparation several times after our first observation [15], with the same qualitative result. The nitrogen species have always been found although their amount varies slightly from one set of samples to another following the slight changes of the Ag amount and/or nanostructure features. These results allow us ruling out the direct adsorption of any nitrile reagent as possible source for the observed nitrile species.

Consequently, the nitrile species must result from a chemical reaction of atmospheric reactants at the Ag nanostructures / a-Al_2O_3 interface. Three compounds can provide the required nitrogen: N_2, NO and NO_2. Among them, the N_2 molecule is the main component of the atmosphere (78%). However, it is chemically inert and is only known to react with some metals (Cr, Si, Ti, Al, B, Be, Mg, Ba Sr, Ca and Li) to produce nitrides at very high temperature, or with O_2, C and H_2 to produce NO, NO_2, HCN and NH_3 at high temperature and high pressure. To our knowledge, it has never been reported the reaction of N_2 at room temperature and atmospheric pressure with Ag, C or Al_2O_3. At present, the reaction at room temperature of the N_2 molecule with transition metals has only been partially reached within the coordination sphere of highly sophisticated organometallic complexes of metals in the Groups 6 to 9 of the Periodic Table and by means of strong reducing agents [49].

Exposure of Ag to dry nitrogen atmosphere was reported to lead to a red-shift of the SPR of Ag NPs, an effect that was explained in terms of activation of N_2 molecules by plasma species (radicals, ions, …) produced prior to the deposition process [50]. In our work, the first exposure to dry N_2 occurs just after sample preparation by PLD to bring the samples to atmospheric pressure. In order to explore if this exposure could play any role on the observed formation of nitrile species, we have produced one sample under the same conditions than the intermediate thickness sample and brought it to atmospheric pressure by filling the vacuum chamber with high purity Ar. No significant differences could be appreciated between the two samples upon aging including the nitrile content [15]. These results and the aforementioned chemical inertness of N_2 lead us to discard reactions of this molecule as responsible for the formation of nitriles.

The next two nitrogen containing gas molecules in the atmosphere, i.e. NO an NO_2, thus become the only realistic potential candidates. These nitrogen oxides, which

are generically named NO_x, are pollutants produced in small quantities during high temperature combustion and their concentration in the air of highly populated cities can reach levels higher than ~$5x10^{-6}$ % (or 50 ppb). In order to reduce this concentration, heterogeneous catalysts that promote the reaction of NO_x with reductant reagents in the atmosphere, like CO, hydrocarbons or alcohols have successfully been developed [51]. Among them, several formulations based on Ag/Al_2O_3 catalysts have proved to be particularly active [48,52–54] and although there is still some speculation about the mechanism for NO_x reduction, -CN and –NCO species have been proposed as key intermediates [46]. According to these authors, when CO is used as reductant, the process starts with the adsorption of CO and NO_x on the same Ag NP where they are both dissociated. Later on, activated C* and N* atoms react and Ag-CN species become formed.

Like nitrogen oxides, CO is also a common pollutant in the air of large urban areas where it reaches concentrations of $3x10^{-3}$ % or 30 ppm that are nearly three orders of magnitude higher than those typically found of NO_x. Consequently, urban air could provide simultaneously the required CO and NO_X to produce the Ag-CN species. However, the great amount of carbon detected on the surface of our samples lead us to consider in addition the existence of adsorbed -CH_x species (hydrocarbons) most likely related to the method used for producing the samples. It is well known that PLD involves high energetic ions that lead to surface sputtering as well as sub-surface metal implantation [55]. For the case of Ag and the laser fluence used in this work to produce the samples, ~25% of the silver species arriving to the substrate have kinetics energies >200 eV [56]. Their bombardment is responsible for the very dense, flat and free from mesopores a-Al_2O_3 layers produced by PLD as reported elsewhere [57]. However, it can also produce oxygen vacancies, coordinately unsaturated Al^{+3} sites and microstructural

defects in the a-Al_2O_3 surface that can act as sites for the chemisorption of hydrocarbons at the vicinity of the Ag nanostructures. Once hydrocarbons become adsorbed, they can migrate to the surface of the Ag NPs where the formation of nitriles will be catalyzed upon exposure to atmosphere.

The hypothesis of hydrocarbons adsorbed in the surface of a-Al_2O_3 instead of CO directly adsorbed on Ag as a reductant of the NO_x species allows us explaining the different concentration of nitriles (catalytic activity) found in the several samples. For both reactants to adsorb it is thus necessary that the amount of Ag is below the percolation limit in order to lead to regions of uncovered a-Al_2O_3 from where the chemisorbed hydrocarbons can later migrate to the surface of the metal. In other words, the reactivity of the system will tend to saturate as the amount of deposited Ag increases and will be blocked once the thickness of the Ag is above a critical value (i.e. above the percolation limit), in agreement with our experimental observations. Further support to this interpretation is provided by the fact that the nitrile surface concentration (N/Ag in Figure 11 and Table 1) is approximately the same in as grown and laser exposed regions in spite of the strong morphological changes induced by the laser treatment on the Ag nanostructure.

The results presented in this work in addition evidence that the optical response of the Ag nanostructures exhibits significant changes upon aging that are stronger the smaller the amount of silver. The main findings can be summarized as follows:

- The SPR wavelength of as grown regions (discontinuous metal layers) blue-shifts upon aging, the smaller the effective thickness of the nanostructures the higher the blue-shift.
- The SPR wavelength of laser exposed regions (isolated and almost spherical NPs) changes much less upon aging than that of as grown regions.

- The extinction at the UV side of the spectrum of both as grown and laser exposed regions increases significantly upon aging in the thinnest sample.

Comparing these findings to the chemical changes and taking into account the fact that the nitrogen incorporation follows the same evolution with time in as grown and laser exposed regions, one can conclude that the changes observed in the wavelength of the SPR are not only linked to the nitrile formation.

It is well known that the SPR wavelength and width are very sensitive to the dimensions and shape of the nanostructures and the SPR generally shifts blue and becomes narrower when the dimensions of the NPs are reduced and/or the NPs approach spheres [58]. This is what we observe in Figure 1 at 0.5 m when comparing laser exposed to as grown regions and this result is consistent with SEM observations (Figure 3 and Figure 5). Upon aging, the most significant structural change is the appearance of elongated features at 7 m in as grown regions of the thinnest sample and at 15 m in the intermediate thickness sample (Figure 3). Comparing their dependence on aging time included in Figure 4a to the dependence of SPR wavelength included in Figure 2, it becomes clear that the changes in the former are not mirrored in the latter. Notice for instance that the elongated features are not observed in the intermediate thickness sample at 7 m (Figure 3e) when a significant shift of the SPR is already observed (Figure 2). It can be thus concluded that the changes in the SPR wavelength are not linked to the appearance of the elongated nanostructures and this result agrees well with our earlier conclusion that the elongated structures have no significant impact on the optical spectra [15]. The origin of these elongated nanostructures and whether they relate to the nitrogen incorporation observed in these samples is at this stage unclear and requires further investigation.

On the one hand, the results obtained from SEM analysis on the features of the underlying nanostructure of the as grown regions over which the elongated structures develop show that the metal coverage is reduced due to metal agglomeration upon aging (Figure 4b). Agglomeration is a process that leads to the morphology of the nanostructures approaching that of spheres and this process should result in a blue-shift of the SPR wavelength as observed in as grown regions upon aging. On the other hand, the formation of a dielectric overlayer on the surface of the metal nanostructures by silver oxidation is expected to lead to a red-shift of the SPR wavelength as has been reported both upon oxidation and sulfurization [13] due to the higher refractive index of the shell material with respect to that of air. However, in our earlier work [15], we have also observed a blue-shift upon aging rather than a red-one. It was suggested that the blue-shift could relate to the much smaller dimensions of NPs with respect to those reported in literature that lead to a red-shift (few nm diameter compared to tens of nm). The smaller dimensions imply that the surface to bulk atoms ratio is very high and when oxidation occurs, an oxidized overlayer grows at the expense of the metal effectively reducing the dimension of the metal core. The effect of this reduction is much stronger than that of the refractive index of the overlayer being higher than that of air thus fully compensating the red-shift. The agglomeration of nanostructures in as grown regions together with the fact that the SPR wavelength of the almost round NPs produced by laser irradiation show a very reduced shift upon aging supports further this conclusion since the surface-to-volume atom ratio is minimum for the almost spherical NPs produced by laser induced dewetting.

The extinction at the UV side of the spectrum increases strongly upon aging in the thinnest sample that is the one that also becomes strongly oxidized. Furthermore, this increase is similarly high in both as grown and laser exposed regions (see Figure

1b) and both regions show similar amount of nitrogen incorporation (see Figure 11). Therefore, the extinction at the UV side of the spectrum must be linked to the chemical changes. Since this extinction has been reported to be a means to distinguish hetero nanostructures such as core-shell structures from nanoalloyed nanostructures [59–61], it provides further support to the formation of an hetero nanostructure formed by a metallic core and a dielectric nitrile overlayer as discussed above. Furthermore, the extinction spectrum of the elements that have been incorporated during aging can be estimated as the difference between the extinction spectrum acquired just after sample deposition and the one after the corrosion process. The result achieved when subtracting the spectra acquired at 0.5 m and 15 m for both the as grown and laser exposed regions of the thinnest sample reveals a monotonous decrease of the extinction in the range 300-800 nm. The result is very similar to that reported for oxidized silver produced by a flow of O_2 on Ag supported on Al_2O_3 annealed at 470 K [62] thus supporting further that the strong UV absorption of the thinnest sample is linked to the oxidation process of silver.

CONCLUSIONS

The main finding of this work is a new corrosion route of Ag nanostructures on a-Al_2O_3 at room temperature and atmospheric conditions that leads to the catalytic production of nitriles. The mechanism is initiated by the adsorption of hydrocarbons at defect sites in the surface of the a-Al_2O_3 layer that supports the Ag nanostructures. These adsorbates migrate to the surface of the metal where NO_x species from the atmosphere are also adsorbed. Their dissociation followed by their reaction lead to the formation of Ag-CN. In our work, the defects in the a-Al_2O_3 support mediating the process are generated during the production of the Ag nanostructures on the a-Al_2O_3 layer by pulsed laser deposition and due to the bombardment of Ag ions having kinetic

energies >200 eV. For this corrosion mechanism to occur, it becomes essential that the a-Al_2O_3 layer is not fully covered by the Ag nanostructure and thus it is the coverage rather than the dimensions the key parameter controlling the efficiency of the corrosion process. It is also worth to point out that when this corrosion mechanism occurs, sulfidation becomes almost negligible.

The corrosion process produces a dielectric overlayer on top of the metal nanostructures that on the one hand, increases the optical extinction of the samples at the UV side of the spectrum. On the other hand, the production of this overlayer occurs at the expense of part of the metal of the nanostructures thus reducing their effective dimensions. However, the aging process involves in addition agglomeration of the metal that makes the features of the nanoparticles to approach those of spheres. The effect of the changes in the dimensions/features of the nanostructures dominates over the effect of the dielectric overlayer finally causing a blue-shift of the SPR wavelength. This work finally shows that the monitoring of the SPR is a very sensitive and easy to use tool for analyzing the corrosion / aging process of metal nanostructures.

ACKNOWLEDGMENTS

R. J. P. acknowledges the grant JCI-2012-13034 from the Juan de la Cierva program.

Authors thank the Spanish Ministry of Science and Innovation (Projects MAT2013-42900-P and MAT2013-40852-R), the “Junta de Andalucía” (Project TEP8067) for financial support.

REFERENCE

[1] Campbell C T 1997 Ultrathin metal films and particles on oxide surfaces: structural, electronic and chemisorptive properties *Surf. Sci. Rep.* **27** 1–111

[2] Sepúlveda B, Angelomé P C, Lechuga L M and Liz-Marzán L M 2009 LSPR-based nanobiosensors *Nano Today* **4** 244–51

[3] Atwater H A and Polman A 2010 Plasmonics for improved photovoltaic devices *Nat. Mater.* **9** 205–13

[4] Soukoulis C M and Wegener M 2011 Past achievements and future challenges in the development of three-dimensional photonic metamaterials *Nat. Photonics*

[5] Yang Y, Pillai S, Mehrvarz H, Kampwerth H, Ho-Baillie A and Green M A 2012 Enhanced light trapping for high efficiency crystalline solar cells by the application of rear surface plasmons *Sol. Energy Mater. Sol. Cells* **101** 217–26

[6] Gorkunov M V, Artemov V V, Yudin S G and Palto S P 2014 Tarnishing of silver subwavelength slit gratings and its effect on extraordinary optical transmission *Photonics Nanostructures - Fundam. Appl.* **12** 122–9

[7] Ouyang Z, Zhao X, Varlamov S, Tao Y, Wong J and Pillai S 2011 Nanoparticle-enhanced light trapping in thin-film silicon solar cells *Prog. Photovoltaics Res. Appl.* **19** 917–26

[8] Kalbacova J, Rodriguez R D, Desale V, Schneider M, Amin I, Jordan R and Zahn D R T 2015 Chemical stability of plasmon-active silver tips for tip-enhanced Raman spectroscopy *Nanospectroscopy* **1**

[9] Opilik L, Dogan Ü, Szczerbiński J and Zenobi R 2015 Degradation of silver near-field optical probes and its electrochemical reversal *Appl. Phys. Lett.* **107** 091109

[10] Sennett R S and Scott G D 1950 The Structure of Evaporated Metal Films and Their Optical Properties *J. Opt. Soc. Am.* **40** 203–11

[11] Bennett H E 1969 Formation and Growth of Tarnish on Evaporated Silver Films *J. Appl. Phys.* **40** 3351

[12] Graedel T E 1992 Corrosion Mechanisms for Silver Exposed to the Atmosphere *J. Electrochem. Soc.* **139** 1963

[13] Wang L, Xiong W, Nishijima Y, Yokota Y, Ueno K, Misawa H, Bi G and Qiu J 2011 Spectral properties and mechanism of instability of nanoengineered silver blocks *Opt. Express* **19** 10640

[14] Mcmahon M D, Lopez R, Meyer H M, Feldman L C and Haglund R F 2005 Rapid tarnishing of silver nanoparticles in ambient laboratory air *Appl. Phys. B* **80** 915–21

[15] Peláez R J, Castelo A, Afonso C N, Borrás A, Espinós J P, Riedel S, Leiderer P and Boneberg J 2013 Enhanced reactivity and related optical changes of Ag nanoparticles on amorphous Al 2 O 3 supports *Nanotechnology* **24** 365702

[16] Campbell C T 2013 The Energetics of Supported Metal Nanoparticles: Relationships to Sintering Rates and Catalytic Activity *Acc. Chem. Res.* **46** 1712–9

[17] Libuda J and Freund H-J 2005 Molecular beam experiments on model catalysts *Surf. Sci. Rep.* **57** 157–298

[18] Meyer R, Ge Q, Lockemeyer J, Yeates R, Lemanski M, Reinalda D and Neurock M 2007 An ab initio analysis of adsorption and diffusion of silver atoms on alumina surfaces *Surf. Sci.* **601** 134–45

[19] Xiao L and Schneider W F 2010 Influence of α-alumina supports on oxygen binding to Pd, Ag, Pt, and Au *Chem. Phys. Lett.* **484** 231–6

[20] Mao B-H, Chang R, Shi L, Zhuo Q-Q, Rani S, Liu X-S, Tyo E C, Vajda S, Wang S-D and Liu Z 2014 A near ambient pressure XPS study of subnanometer silver clusters on Al 2 O 3 and TiO 2 ultrathin film supports *Phys. Chem. Chem. Phys.* **16** 26645–52

[21] Bulanin K M, Lavalley J C and Tsyganenko A A 1995 Infrared Study of Ozone Adsorption on TiO2 (Anatase) *J. Phys. Chem.* **99** 10294–8

[22] Katiyar P, Jin C and Narayan R J 2005 Electrical properties of amorphous aluminum oxide thin films *Acta Mater.* **53** 2617–22

[23] Mardare A I, Kaltenbrunner M, Sariciftci N S, Bauer S and Hassel A W 2012 Ultra-thin anodic alumina capacitor films for plastic electronics *Phys. status solidi* **209** 813–8

[24] Valant M, Luin U, Fanetti M, Mavrič A, Vyshniakova K, Siketić Z and Kalin M 2016 Fully Transparent Nanocomposite Coating with an Amorphous Alumina Matrix and Exceptional Wear and Scratch Resistance *Adv. Funct. Mater.* **26** 4362–9

[25] Rodríguez C E, Peláez R J, Afonso C N, Riedel S, Leiderer P, Jimenez-Rey D and Climent-Font A 2014 Plasmonic response and transformation mechanism upon single laser exposure of metal discontinuous films *Appl. Surf. Sci.* **302** 32–6

[26] Shirley D A 1972 High-Resolution X-Ray Photoemission Spectrum of the Valence Bands of Gold *Phys. Rev. B* **5** 4709–14

[27] Tanuma S, Powell C J and Penn D R 2011 Calculations of electron inelastic mean free paths. IX. Data for 41 elemental solids over the 50 eV to 30 keV range *Surf. Interface Anal.* **43** 689–713

[28] Scofield J H 1976 Hartree-Slater subshell photoionization cross-sections at 1254 and 1487 eV *J. Electron Spectros. Relat. Phenomena* **8** 129–37

[29] D.Briggs and M.P.Seah 1983 *Practical Surface Analysis by Auger and X-ray Photoelectron Spectroscopy (Apendix 4. 477-509)* (Chichester: Wiley.)

[30] Ferraria A M, Carapeto A P and do Rego A M B 2012 X-ray photoelectron spectroscopy: Silver salts revisited *Vacuum* **86** 1988–91

[31] Hashimoto S, Uwada T, Hagiri M, Takai H and Ueki T 2009 Gold Nanoparticle-Assisted Laser Surface Modification of Borosilicate Glass Substrates *J. Phys. Chem. C* **113** 20640–7

[32] Luo K, St. Clair T P, Lai X and Goodman D W 2000 Silver Growth on TiO 2 (110) (1 × 1) and (1 × 2) *J. Phys. Chem. B* **104** 3050–7

[33] Oates T W H, Losurdo M, Noda S and Hinrichs K 2013 The effect of atmospheric tarnishing on the optical and structural properties of silver nanoparticles *J. Phys. D. Appl. Phys.* **46** 145308

[34] Lindquist J M, Ziegler J P and Hemminger J C 1989 Photoelectron spectroscopy studies of the hydrogenation of cyanogen on Pt(111): Comparison with HCN and ethylenediamine *Surf. Sci.* **210** 27–45

[35] Kennou S, Logothetidis S, Sygellou L, Laskarakis A, Sotiropoulou D and Panayiotatos Y 2002 Variation of nitrogen incorporation and bonding configuration of carbon nitride films studied by X-ray photoelectron spectroscopy (XPS) and Fourier transform infrared (FT-IR) spectroscopic ellipsometry *Diam. Relat. Mater.* **11** 1183–7

[36] Hanks T W, Ekeland R A, Emerson K, Larsen R D and Jennings P W 1987 Reactions of diazomethane derivatives with platinum(II): a facile method for platinum ylide preparation *Organometallics* **6** 28–32

[37] Gouttebaron R, Bourgeois S and Perdereau M 2000 Study by static SIMS, XPS and UPS of the adsorption of cyanogen on (100) Ni surfaces *Surf. Sci.* **458** 239–46

[38] Ibrado A S and Fuerstenau D W 1995 Infrared and X-ray photoelectron spectroscopy studies on the adsorption of gold cyanide on activated carbon *Miner. Eng.* **8** 441–58

[39] Motamedi P and Cadien K 2014 XPS analysis of AlN thin films deposited by plasma enhanced atomic layer deposition *Appl. Surf. Sci.* **315** 104–9

[40] Pérez Taborda J A, Caicedo J C, Grisales M, Saldarriaga W and Riascos H 2015 Deposition pressure effect on chemical, morphological and optical properties of binary Al-nitrides *Opt. Laser Technol.* **69** 92–103

[41] Shanley E S and Ennis J L 1991 The chemistry and free energy of formation of silver nitride *Ind. Eng. Chem. Res.* **30** 2503–6

[42] Titantah J T and Lamoen D 2007 Carbon and nitrogen 1s energy levels in amorphous carbon nitride systems: XPS interpretation using first-principles *Diam. Relat. Mater.* **16** 581–8

[43] Kaufman J H, Metin S and Saperstein D D 1989 Symmetry breaking in nitrogen-doped amorphous carbon: Infrared observation of the Raman-active G and D bands *Phys. Rev. B* **39** 13053–60

[44] Ciszek J W and Tour J M 2005 Mechanistic Implications of the Assembly of Organic Thiocyanates on Precious Metals *Chem. Mater.* **17** 5684–90

[45] El-Hinnawi M A, Peter L and Meyer B 1985 Raman spectra of copper(I), silver(I) and gold(I) cyanides in aqueous solutions of sodium thiosulphate *J. Raman Spectrosc.* **16** 272–9

[46] Thibault-Starzyk F, Seguin E, Thomas S, Daturi M, Arnolds H and King D A 2009 Real-Time Infrared Detection of Cyanide Flip on Silver-Alumina NOx Removal Catalyst *Science (80-.).* **324** 1048–51

[47] Miquel P, Granger P, Jagtap N, Umbarkar S, Dongare M and Dujardin C 2010 NO reduction under diesel exhaust conditions over Au/Al2O3 prepared by deposition-precipitation method *J. Mol. Catal. A Chem.* **322** 90–7

[48] Bion N, Saussey J, Haneda M and Daturi M 2003 Study by in situ FTIR

spectroscopy of the SCR of NOx by ethanol on Ag/Al2O3—Evidence of the role of isocyanate species *J. Catal.* **217** 47–58

[49] Khoenkhoen N, de Bruin B, Reek J N H and Dzik W I 2015 Reactivity of Dinitrogen Bound to Mid- and Late-Transition-Metal Centers *Eur. J. Inorg. Chem.* **2015** 567–98

[50] Antad V, Simonot L and Babonneau D 2013 Tuning the surface plasmon resonance of silver nanoclusters by oxygen exposure and low-energy plasma annealing *Nanotechnology* **24** 045606

[51] Granger P and Parvulescu V I 2011 Catalytic NO x Abatement Systems for Mobile Sources: From Three-Way to Lean Burn after-Treatment Technologies *Chem. Rev.* **111** 3155–207

[52] Kim P S, Cho B K, Nam I-S and Choung J W 2014 Bifunctional Ag-based catalyst for NO x reduction with E-diesel fuel *ChemCatChem* **6** 1570–4

[53] Martin N M, Erdogan E, Grönbeck H, Mikkelsen A, Gustafson J and Lundgren E 2014 Toward a Silver–Alumina Model System for NO x Reduction Catalysis *J. Phys. Chem. C* **118** 24556–61

[54] Ralphs K, Chansai S, Hardacre C, Burch R, Taylor S F R and James S L 2015 Mechanochemical preparation of Ag catalysts for the n-octane-SCR de-NOx reaction: Structural and reactivity effects *Catal. Today* **246** 198–206

[55] Perea A, Gonzalo J, Budtz-Jo□rgensen C, Epurescu G, Siegel J, Afonso C N and García-López J 2008 Quantification of self-sputtering and implantation during pulsed laser deposition of gold *J. Appl. Phys.* **104** 084912

[56] Baraldi G, Perea A and Afonso C N 2011 Dynamics of ions produced by laser ablation of several metals at 193 nm *J. Appl. Phys.* **109** 043302

[57] Castelo A, Afonso C N, Pesce E and Piscopiello E 2012 The importance of the energetic species in pulsed laser deposition for nanostructuring. *Nanotechnology* **23** 105603

[58] Lee K-C, Lin S-J, Lin C-H, Tsai C-S and Lu Y-J 2008 Size effect of Ag nanoparticles on surface plasmon resonance *Surf. Coatings Technol.* **202** 5339–42

[59] Xiao-Yong G, Hong-Liang F, Jiao-Min M and Zeng-Yuan Z 2010 Spectroscopic ellipsometric study of the optical properties of Ag 2 O film prepared by direct-

current magnetron reactive sputtering *Chinese Phys. B* **19** 90701

[60] Encina E R and Coronado E A 2010 On the Far Field Optical Properties of Ag−Au Nanosphere Pairs *J. Phys. Chem. C* **114** 16278–84

[61] Sheikholeslami S, Jun Y, Jain P K and Alivisatos A P 2010 Coupling of Optical Resonances in a Compositionally Asymmetric Plasmonic Nanoparticle Dimer *Nano Lett.* **10** 2655–60

[62] Sazama P, Capek L, Drobna H, Sobalik Z, Dedecek J, Arve K and Wichterlova B 2005 Enhancement of decane-SCR-NO over Ag/alumina by hydrogen. Reaction kinetics and in situ FTIR and UV–vis study *J. Catal.* **232** 302–17

Table 1: Silver photoelectronic energy parameters ($Ag_{3d5/2}$ binding energy, Ag_{M4VV} kinetic energy and silver modified Auger parameter (α^*)), percentage of silver in metallic state (Ag(0)), surface composition (atomic %) and some relevant atomic ratios obtained from X-ray photoemission spectral peaks for both as grown and laser exposed regions at different aging stages.

Samples			$Ag_{3d5/2}$		Ag_{M4VV} (*)	α^* (eV)	% Ag(0)	Surface Composition (Atomic %)						Atomic ratios			
	Time (m)	Thick (nm)	Binding Energy (eV)	FWHM (eV)	Kinetic Energy (eV)	Ag(0) Ag(I)		O	Al	Ag	C	N	S	Ag/Al	N/Ag	S/Ag	O/(1/2Ag +3/2Al)
As grown	0.5	1.6	368.4	1.60	357.1	725.5	100	30.7	17.8	14.6	36.9	0.0	0.0	0.83	0.0	0.0	0.90
		3.7	368.3	1.45	357.3	725.6	100	29.3	13.7	21.2	35.8	0.0	0.0	1.57	0.0	0.0	0.94
		5.9	368.2	1.40	357.5	725.7	100	18.1	8.3	25.1	48.5	0.0	0.0	3.07	0.0	0.0	0.72
	7	1.6	368.7	2.15	357.3 353.3	726.0 722.0	40	19.1	11.3	14.5	50.8	3.9	0.4	1.28	0.27	0.03	0.79
		3.7	368.3	1.65	357.5	725.8	100	17.8	9.0	23.6	46.9	2.3	0.4	2.61	0.10	0.02	0.70
		5.9	368.3	1.40	357.6	725.9	100	15.6	5.6	26.9	50.5	1.4	0.3	4.68	0.05	0.01	0.71
	15	1.6	368.9	2.00	357.2 353.2	726.1 722.1	20	17.2	11.0	15.1	50.0	6.2	0.4	1.36	0.41	0.03	0.71
		3.7	368.3	1.85	357.5	725.8	75	16.6	9.0	20.3	51.3	2.5	0.3	2.25	0.13	0.02	0.70
		5.9	368.3	1.40	357.5	725.8	100	15.1	6.0	27.0	50.0	1.4	0.4	4.32	0.05	0.02	0.67
	20	1.6	368.9	2.00	357.2 353.2	726.1 722.1	20	16.6	10.6	14	52.9	5.4	0.5	1.32	0.39	0.04	0.72
		3.7	368.3	1.85	357.5	725.8	75	13.6	6.4	19.0	58.2	2.4	0.4	2.97	0.12	0.02	0.71
		5.9	368.3	1.40	357.5	725.8	100	12.2	4.25	22.0	59.5	1.5	0.6	5.1	0.06	0.03	0.70
Laser exposed	0.5	1.6	368.3	1.45	357.1	725.4	100	34.0	21.8	10.7	33.5	0.0	0.0	0.49	0.0	0.0	0.89
		5.9	368.4	1.30	357.2	725.6	100	30.9	20.6	12.6	35.9	0.0	0.0	0.62	0.0	0.0	0.83
	7	1.6	368.1	1.95	357.4	725.5	90	24.8	15.9	13.3	43.5	2.1	0.4	0.84	0.16	0.03	0.84
		5.9	368.3	1.30	357.4	725.7	100	24.2	15.5	13.9	45.7	0.4	0.3	0.90	0.03	0.02	0.80
	15	1.6	368.6	2.30	357.1 353.1	725.6 721.7	40	17.0	10.5	10.3	57.6	4.1	0.4	0.98	0.41	0.04	0.81
		5.9	368.2	1.30	357.5	725.7	100	21.6	14.9	16.5	46.3	0.5	0.3	1.11	0.03	0.02	0.70

Table 2: C_{1s} fitting parameters of photoemission peak for as grown regions of the 1.6 nm thick sample at different aging stages.

Time (m)	C_I			C_{II}			C_{III}			C_{IV}			$\Delta C_{II}/\Delta N$
	Energy (eV)	FWHM (eV)	%	Energy (eV)	FWHM (eV)	%	Energy (eV)	FWHM (eV)	%	Energy (eV)	FWHM (eV)	%	
0.5	284.6	1.6	72.3	285.3	1.6	16.8	286.8	1.6	3.8	288.1	2.1	7.1	0
7	284.7	1.6	66.0	285.3	1.6	24.2	286.6	1.6	4.7	288.3	2.1	5.0	1.6
15	284.7	1.6	64.7	285.4	1.6	26.4	286.8	1.6	4.6	288.5	2.1	4.3	1.1

FIGURE CAPTIONS

FIGURE 1.

Extinction spectra of (full line) as grown and (dashed lines) laser exposed regions at F=152 mJcm^{-2} of the (a) 5.9 nm and (b) 1.6 nm thick samples and measured at (black) 0.5 m and (grey) 15 m. SEM images at same magnification of the nanostructure of the thickest sample at 0.5 m (c) as grown and laser exposed regions at (d) 145 mJcm^{-2}, (e) 158 mJcm^{-2} and (f) 196 mJcm^{-2}. The inset shows the evolution of the SPR wavelength as a function of laser exposure fluence in the thickest sample at (black) 0.5 m and (grey) 15 m; the SPR values at 0 fluence correspond to as grown regions.

FIGURE 2.

SPR wavelength as a function of aging time for (full lines and symbols) as grown and (dashed lines and open symbols) laser exposed regions at 152 mJcm^{-2} in the (●,○) 5.9 nm, (◆) 3.7 nm and (▲,△) 1.6 nm thick samples. Lines are guidelines.

FIGURE 3.

SEM images at same magnification of as grown regions of the (a-c) 1.6 nm, (d-f) 3.7 nm and (g-i) 5.9 nm thick samples after (a,d,g) 0.5 m, (b,e,h) 7 m and (c,f,i) 15 m.

FIGURE 4.

(a) (full symbols and lines) Mean Feret length and (open symbols and dashed lines) aspect ratio of the elongated structures seen in Figure 3b and 3c and f as a function of aging stage for as grown regions of the (▲,△) 1.6 nm and (◆,◇) 3.7 nm thick samples. (b) Metal coverage and (c) mean Feret diameter of the nanostructures seen in SEM images as a function of aging stage for (full symbols and lines) as grown and (open symbols and dashed line) laser regions of the (◆) 3.7 nm and (●,○) 5.9 nm thick samples. Lines are guidelines.

FIGURE 5.

SEM images at same magnification of laser exposed regions of the (a,b) 1.6 nm and (c,d) 5.9 nm thick samples after (a,c) 0.5 m and (b,d) 15 m.

FIGURE 6.

X-ray photoemission survey spectra of as grown regions of the 1.6 nm thick sample at (black) 0.5 m and (grey) 7 m.

FIGURE 7.

High energy resolution X-ray photoemission spectral region of (a,c) Ag_{3d} and (b,c) Ag_{MNN} at 0.5 m of the (a, b) as grown and (c, d) laser exposed regions of the (green) 1.6 nm, (red) 3.7 nm and (black) 5.9 nm thick samples.

FIGURE 8.

High energy resolution X-ray photoemission spectral regions of (a) Ag_{3d} and (b) Ag_{MNN}, of as grown regions of the 1.6 nm thick sample at (black) 0.5 m, (red) 7 m and (green) 15 m and (blue) oxidized reference sample.

FIGURE 9.

High energy resolution X-ray photoemission spectral regions of (a) S_{2p}, (b) C_{1s} and (c) N_{1s} collected from as grown regions of the 1.6 nm thick sample at (black) 0.5 m, (red) 7 m and (green) 15 m.

FIGURE 10.

Ag to Al atomic ratio as a function of thickness for (full symbols and lines) as grown and (open symbols and dashed lines) laser exposed regions at (■,□) 0.5 m and (●,○) 7 m. Lines are guidelines.

FIGURE 11.

N to Ag atomic ratio as a function of aging stage for (full symbols and lines) as grown and (open symbols and dashed lines) laser exposed regions of the (●,○) 5.9 nm, (◆) 3.7 nm and (▲,△) 1.6 nm thick samples. Lines are guidelines.

FIGURE 12.

Raman spectra of as grown regions at 7 m of the (black) 5.9 nm and (green) 1.6 nm thick samples (full line) with and (dashed line) without a-Al_2O_3 buffer layer.

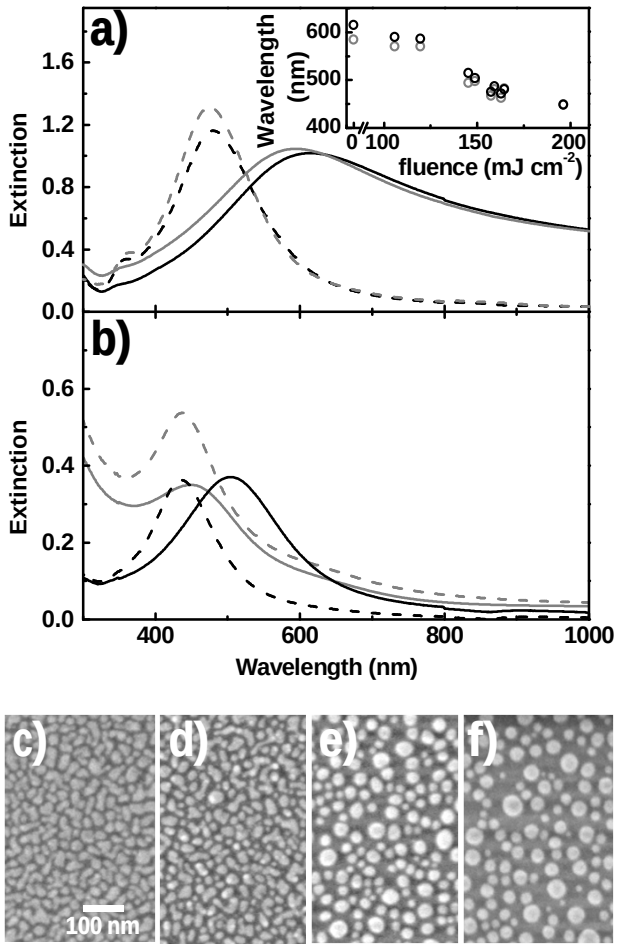

Figure 1

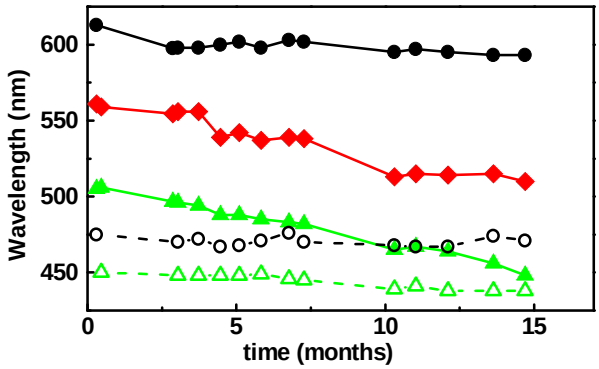

Figure 2

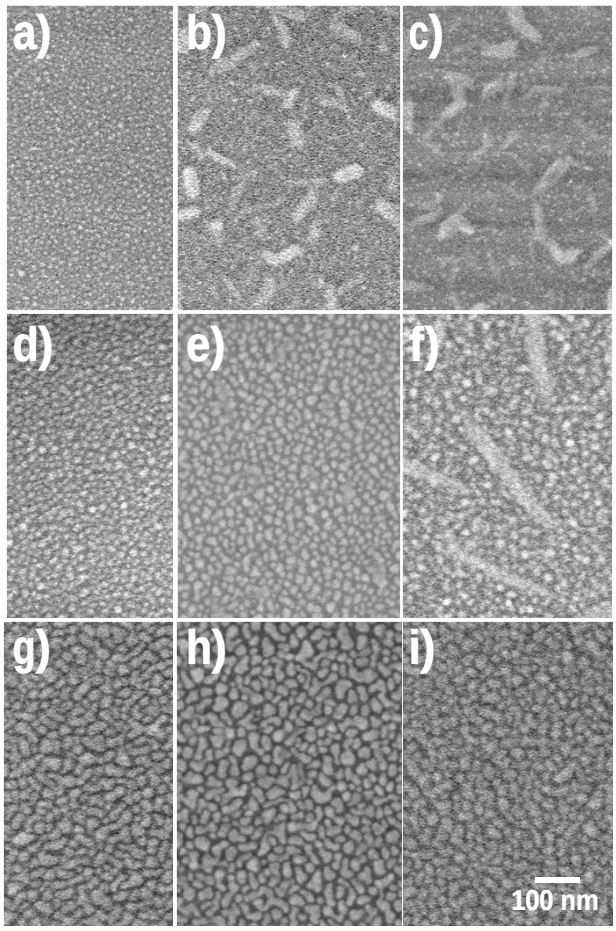

Figure 3

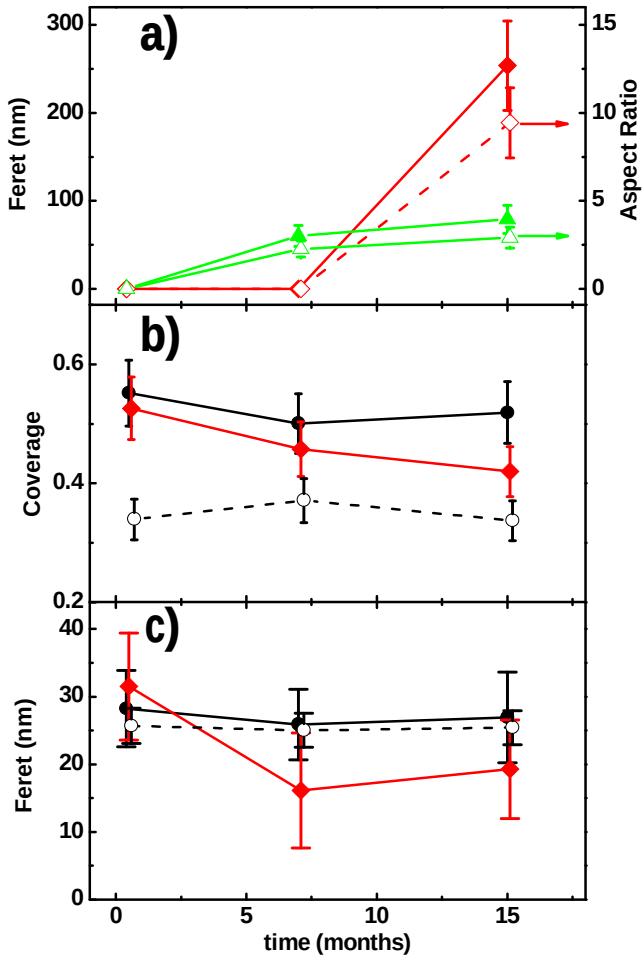
a)
b)
c)
Feret (nm)
Aspect Ratio
Coverage
Feret (nm)
time (months)
300
200
100
0
15
10
5
0
0.6
0.4
0.2
40
30
20
10
0
0
5
10
15

Figure 4

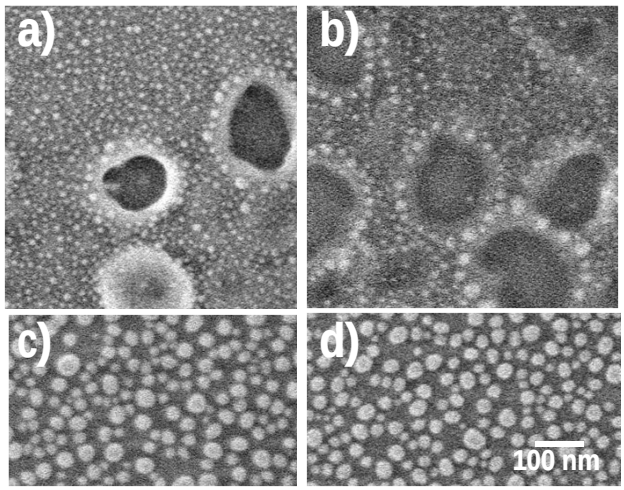

Figure 5

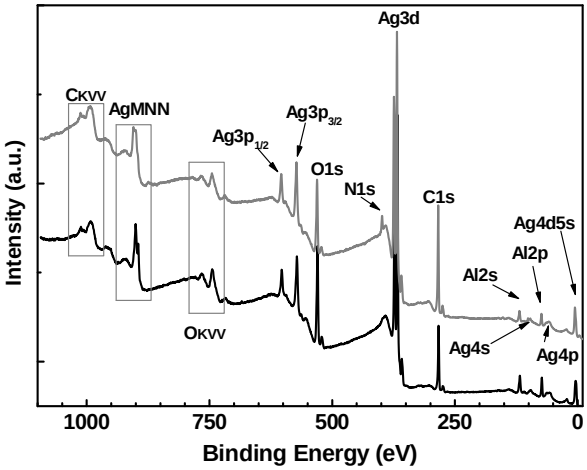
Ag3d
CKVV
AgMNN
Ag3p1/2
Ag3p3/2
O1s
N1s
C1s
Ag4d5s
Al2p
Al2s
Ag4s
Ag4p
OKVV
Intensity (a.u.)
1000
750
500
250
0
Binding Energy (eV)

Figure 6

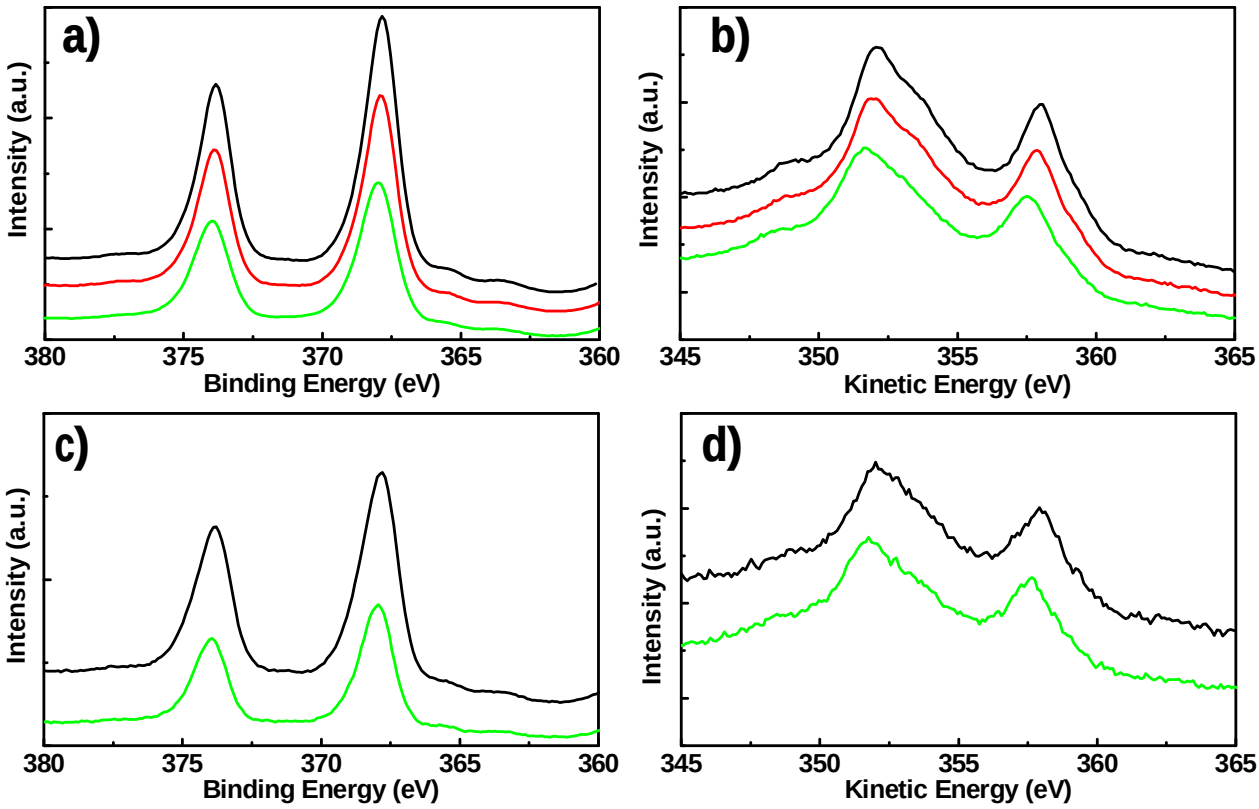
a)
Intensity (a.u.)
380
375
370
365
360
Binding Energy (eV)
b)
Intensity (a.u.)
345
350
355
360
365
Kinetic Energy (eV)
c)
Intensity (a.u.)
380
375
370
365
360
Binding Energy (eV)
d)
Intensity (a.u.)
345
350
355
360
365
Kinetic Energy (eV)

Figure 7

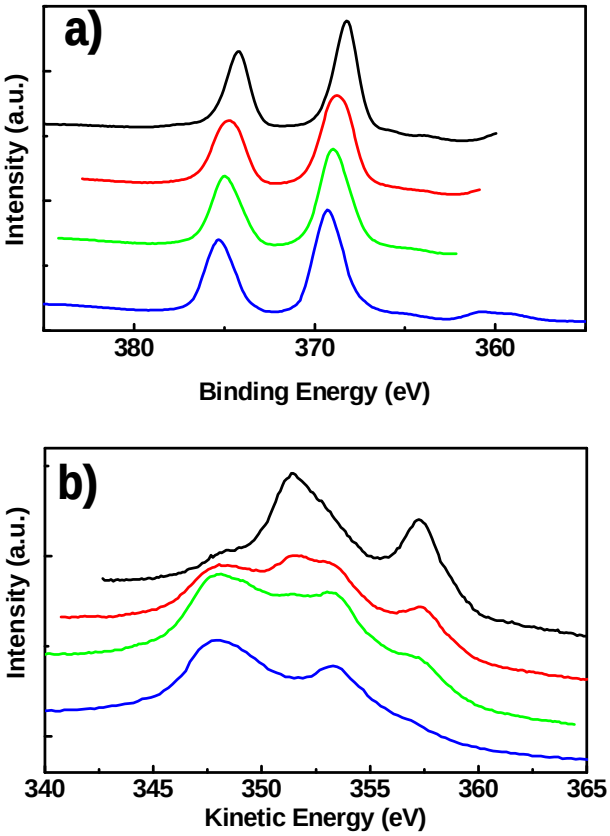
a)
Intensity (a.u.)
380
370
360
Binding Energy (eV)
b)
Intensity (a.u.)
340
345
350
355
360
365
Kinetic Energy (eV)

Figure 8

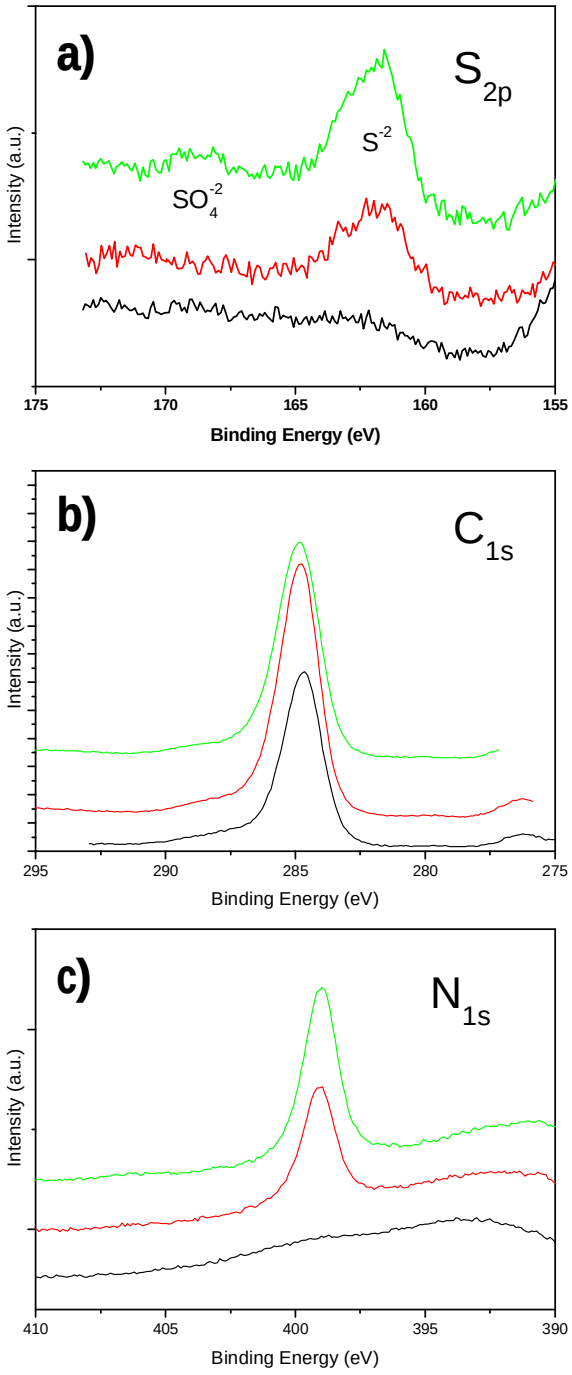
a)
S2p
S-2
SO4-2
Intensity (a.u.)
175
170
165
160
155
Binding Energy (eV)
b)
C1s
Intensity (a.u.)
295
290
285
280
275
Binding Energy (eV)
c)
N1s
Intensity (a.u.)
410
405
400
395
390
Binding Energy (eV)

Figure 9

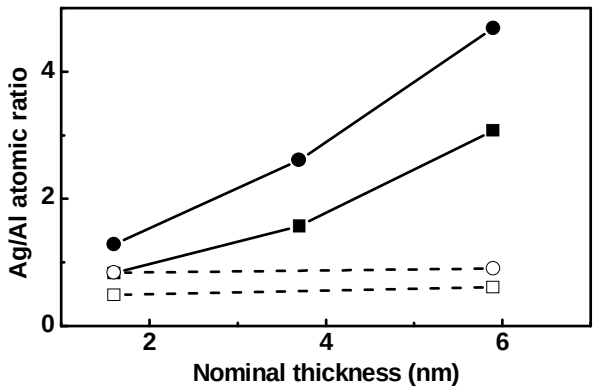

Figure 10

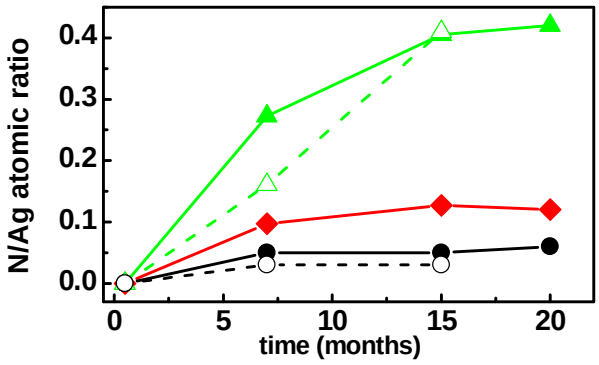

Figure 11

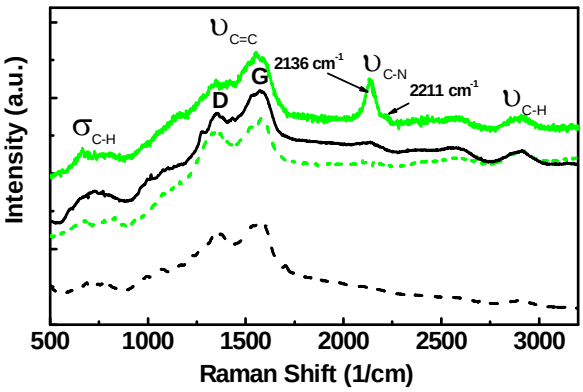
υC=C
2136 cm-1
υC-N
2211 cm-1
υC-H
G
D
σC-H
Intensity (a.u.)
500
1000
1500
2000
2500
3000
Raman Shift (1/cm)

Figure 12

Formation of nitrile species on Ag nanostructures supported on a-Al_2O_3: a new corrosion route for silver exposed to the atmosphere

R.J. Peláez,[1] J. P. Espinós,[2] C.N. Afonso[1]

[1]Laser Processing Group, Instituto de Optica, CSIC, Serrano 121, 28006, Madrid, Spain
[2]Surface Analysis Lab, Instituto de Ciencia de Materiales de Sevilla, CSIC-US, Américo Vespucio 49, 41092, Sevilla, Spain

Electronic Supplementary Information

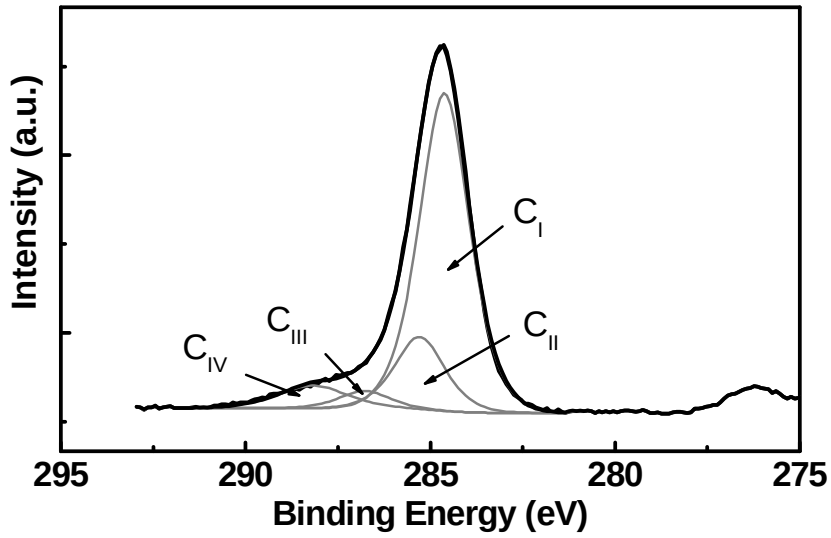

FIGURE S1.
Fitting analysis of the C_{1s} photoemission spectral region of as grown regions of the thinnest sample at 0.5 m. See text for assignation of the carbon chemical states.